Photoelectron dispersion in metallic and insulating VO₂ thin films

Viktor Jonsson ⬤, Luca Piazza ⬤, Martin Månsson ⬤, Jonas Weissenrieder ⬤,[*] and Oscar Tjernberg ⬤[†]

Materials and Nano Physics, KTH Royal Institute of Technology, Hannes Alfvéns väg 12, 11419 Stockholm, Sweden

Sergiy Khartsev ⬤

Division of Electronics and Embedded Systems, KTH Royal Institute of Technology, Electrum 229, 16440 Kista, Stockholm, Sweden

Yasmine Sassa ⬤

Department of Physics, Chalmers University of Technology, 41296 Göteborg, Sweden

Daniel G. Mazzone ⬤

Laboratory for Neutron Scattering and Imaging, Paul Scherrer Institut, 5232 Villigen PSI, Switzerland

Nicolas Gauthier ⬤

Laboratory for Scientific Developments and Novel Materials, Paul Scherrer Institut, 5232 Villigen PSI, Switzerland

Matthias Muntwiler ⬤

Photon Science Division, Paul Scherrer Institut, 5232 Villigen PSI, Switzerland

Chin Shen Ong ⬤, Diana Iuşan ⬤, and Patrik Thunström ⬤

Department of Physics and Astronomy, Uppsala University, Box 516, 75120 Uppsala, Sweden

Olle Eriksson ⬤

Department of Physics and Astronomy, Uppsala University, Box 516, 75120 Uppsala, Sweden
and School of Science and Technology, Örebro University, Fakultetsgatan 1, 701 82 Örebro, Sweden

The underlying mechanism behind the metal-to-insulator transition in VO₂ is still a topic of intense debate. The two leading theoretical interpretations associate the transition with either electron-lattice or electron-electron correlations. Novel experimental results are required to converge towards one of the two scenarios. Here we report on a temperature-dependent angle-resolved photoelectron study of VO₂ thin films across the metal-to-insulator transition. The obtained experimental results are compared to density functional theory calculations. We find an overall energy shift and compression of the electronic band structure across the transition while the overall band topology is conserved. The results demonstrate the importance of electron-electron correlations in establishing the insulating state.

I. INTRODUCTION

Materials hosting a metal-to-insulator transition (MIT) are appealing for many technical applications, as they can be used in electrical switching devices [1,2]. In 1959 Morin [3] discovered that bulk VO₂ exhibits such a transition near room temperature. This is particularly interesting because the material is low cost and hosts potential for ultrafast opti-

cal switching [3–9]. The intriguing nature of the transition, combined with the potential for applications, has motivated considerable research into the material [10–12]. Even though VO₂ is one of the most frequently studied transition-metal oxides, the lack of natural cleavage planes and complications in obtaining high-quality thin-film surfaces have hindered experimental electronic band structure analysis. Hitherto, only a few groups have successfully conducted angle-resolved photoelectron spectroscopy (ARPES) measurements of the material [13–15]. In 2005, Shigemoto *et al.* detected the opening of an insulating gap [16] in bulk VO₂, which was later attributed [17,18] to a splitting of the V $3d$ band into bonding and antibonding d bands parallel to the long (110) axis of the oxygen octahedra. One d band ($d_\parallel$) is located at a binding energy E_{bin} of 0.9 eV, while the other one ($d_\parallel^*$) resides above the Fermi level. Photoelectron data on metallic VO₂ supported the existence of two electron pockets originating

[*]jonas@kth.se
[†]oscar@kth.se

TABLE I. Stable and metastable phases of VO_2.

Phase	Symmetry	Space group
Rutile (R)[a]	$P4_2/mnm$	136
Monoclinic (M_1)[b]	$P2_1/c$	14
Monoclinic (M_2)[c]	$C2/m$	12
Monoclinic (M_3)[d]	$P2/m$	10
Tetragonal (LTP)[e]	$P4/ncc$	130
Tetragonal (HTP)[e]	$I4$, $I\bar{4}$, $I4/m$	79, 82, 87

[a]Reference [23].
[b]Reference [24].
[c]Reference [25].
[d]Reference [26].
[e]Reference [27]. LTP means low temperature phase and HTP means high temperature phase.

from the π^* band of the V $3d$ orbital located ~ 0.4 eV below the Fermi level at the center of the Brillouin zone (Γ) [13]. More recently, ARPES results from thin films indicated the existence of three different bands at Γ, featuring minima at $E_{bin} = 60$, 160, and 340 meV [15]. The authors further reported a substantial Fermi surface nesting which, together with earlier experimental and theoretical studies [19–22], suggests that a charge-density wave instability is involved in the MIT mechanism.

Vanadium oxide compounds exist in several oxidation states, with VO_2 being the only compound that is inconsistent with the general formula $V_nO_{2n\pm1}$. Depending on strain and temperature, the material crystallizes in eight different crystal phases that are summarized in Table I. All of them possess atomic structures that resemble the rutile (R) structure with additional small atomic displacements, changing the unit cell symmetry.

The MIT in bulk VO_2 causes the metallic rutile crystal structure ($a_R = b_R = 4.56$ Å and $c_R = 2.85$ Å) to become monoclinic (M_1) below $T_c = 340$ K [28]. In VO_2 thin films, grown on TiO_2 substrates, the in-plane tensile stress affects this transition by lowering T_c, and films below 74 nm seem to favor a tetragonal over a monoclinic insulating phase [29]. Below the critical thickness [30] of 27 nm Yang *et al.* [31] claimed that the structural transition is suppressed, resulting in ultrathin films being tetragonal both below and above the MIT. However, this claim was contradicted by Gray *et al.* [32], who observed a structural transition in 10-nm-thick films deposited on TiO_2. Most likely, as the thickness of these films decreases, electron-electron correlations ramp up due to dimensional crossover effects, and structural instabilities are dampened until they are fully suppressed below ~ 1 nm [33].

Exact values of the internal coordinates in the tetragonal phase are not known. However, they should be well approximated by a metallic rutile phase in our case as our films are close to the critical limit, i.e., 20 nm. The atomic structure of rutile VO_2 and its corresponding Brillouin zone (BZ) are shown in Fig. 1. For the insulating phase it is possible to use the M_1 phase as the basis for our calculations. By using $\boldsymbol{a}_M = (a_R, 0, -c_R)$, $\boldsymbol{b}_M = (0, a_R, 0)$, and $\boldsymbol{c}_M = (0, 0, 2c_R)$ [21], which hold within 1% relative accuracy, one can project the calculations onto the rutile phase BZ (see Fig. 2).
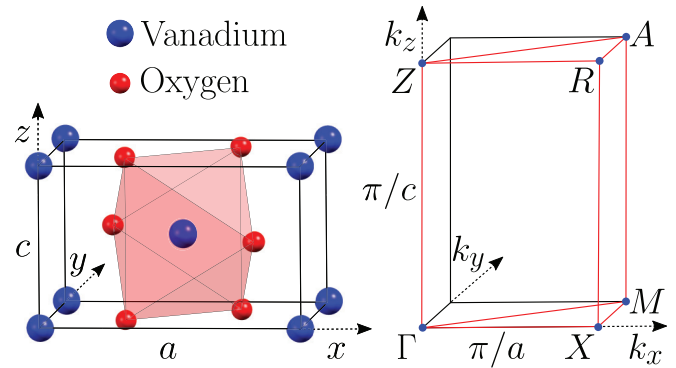

FIG. 1. Structural model (left) and one octant of the Brillouin zone (right) for rutile VO_2. The sizes of vanadium (blue) and oxygen atoms (red) are not to scale. High-symmetry points are indicated in the BZ.

The band structure of VO_2 consists of V $3d$ and O $2p$ bands, which have been studied extensively via theoretical models [12,21,34]. The predominant interpretation of the metallic band structure is that the octahedral crystal field splits the V $3d$ band into higher-energy e_g^σ levels and lower-energy t_{2g} states that reside around the Fermi level. The latter further splits into an antibonding π^* band and a $d_\parallel$ band at lower energies. Below the phase transition the vanadium atoms dimerize, which results in an additional separation of the $d_\parallel$ band. Under compressive strain, VO_2 can stabilize an insulating M_2 phase [35]. Here, only half of the metal ions dimerize, resulting in an antiferromagnetic state that is believed to contribute to the formation of the insulating band gap [21]. We note that all of the aforementioned phases are found close to ambient conditions, which makes the free-energy landscape of the material both difficult to navigate and interesting. To what extent electron-electron (Mott) and electron-lattice (Peierls) correlations are
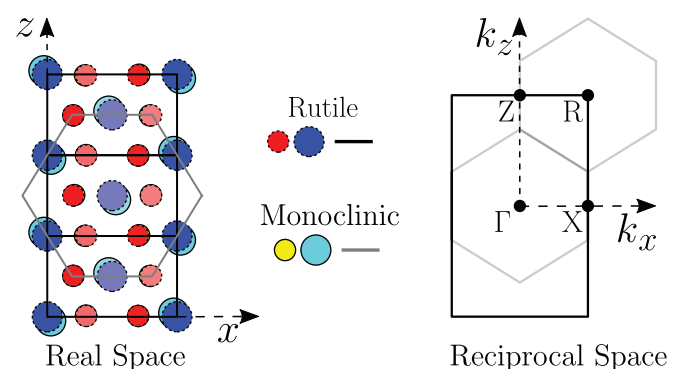

FIG. 2. Atomic positions in VO_2 alongside its BZ projected onto the xz plane. Borders of the conventional unit cell are illustrated in black and gray for the rutile and monoclinic phases, respectively. Note that for the rutile structure, three unit cells are shown. The oxygen and vanadium atoms in the rutile phase are represented by red and blue circles with dashed borders. The corresponding atoms in the monoclinic phase are represented by yellow and cyan circles with solid borders. The color brightness for each atom increases with its y position. Sphere sizes were chosen arbitrarily, but the atomic displacements are scaled to the lattice dimensions.

responsible for the MIT under the different conditions is still an area of intense research and debate [36–41].

Detailed measurements of the electronic band structure through ARPES are a natural step to get further insight into the changes in the VO$_2$ valence band structure across the transition and would shed light on the open questions regarding its nature. Here we present results from ARPES measurements on VO$_2$ films at temperatures above and below T_c. Presenting data from both phases concurrently allows direct comparison between the metallic and insulating band structures of VO$_2$. The results are compared to density functional theory (DFT) calculations performed in the rutile structure for the high-temperature phase (HTP) and in the M_1 structure for the low-temperature phase (LTP). The differences of the high- and low-temperature phases in real and reciprocal spaces are illustrated in Fig. 2.

II. EXPERIMENT

The 20-nm-thick VO$_2$ films were grown with pulsed laser deposition on 5×5 mm^2 TiO$_2$ (001) substrates (CrysTec GmbH). A ceramic V$_2$O$_5$ (99.99%) target was ablated using a Lambda Physik-Compex-110 KrF 248-nm excimer laser with an energy density of 2 J/cm^2 and pulse repetition rate of 20Hz. The oxygen pressure was kept at 15 mTorr during deposition. A film growth rate of 0.32 Å/shot was observed at a substrate-to-target distance of 65 mm while keeping the sample at 375 °C. No postannealing was employed. After deposition, the film was cooled to room temperature within a 15-mTorr oxygen environment. The temperature-dependent resistance was measured in a four-point probe setup using a Keithley 2410 source meter and a Keithley 2002 multimeter with low-frequency alternating current (see Fig. 3). The deposition rate was calibrated by measurements of the thickness using a control film with a KLA-Tencor P-15 profiler.

Cu $K\alpha_1$ ($\lambda = 1.5406$ Å) x-ray diffraction θ-2θ scans revealed a tetragonal single phase for both the substrate and film. The film is strained along the c axis with less than 0.2% compared to the bulk VO$_2$, whose geometry consequently was used in the analysis of the data and in the calculations.

Five samples were transferred into a vacuum suitcase and transported to the Photoemission and Atomic Resolution Laboratory (PEARL) of the Swiss Light Source (SLS) at the Paul Scherrer Institut (PSI), Switzerland. They were clamped on tantalum sample plates using Ta clips and inserted into the PEARL end station. Photoelectron spectroscopy measurements were performed at a base pressure of 1×10^{-10}mbar using photon energies between 60 and 300 eV, corresponding to an electron escape depth of 5 to 10 Å. A series of angular resolved spectra was recorded in steps of 5 eV. A finer step size of 0.5 eV was chosen around specific photon energies. The analyzer slit had vertical and horizontal nominal acceptance ranges of $\pm 30°$ and $\pm 0.25°$, respectively. However, as count rates drop significantly above $\pm 20°$, we limit $k_\parallel$ to within $\pm 5\pi/2a$, which corresponds to $\pm 17°$. The overall energy resolution during the experiment was estimated to 90 meV at $E_{ph} = 60$ eV and 210 meV at $E_{ph} = 270$ eV [42]. The photon beam was continuously scanned across the sample during measurement to avoid photon beam induced degradation. The spectra were recorded at 280 and 340 K,
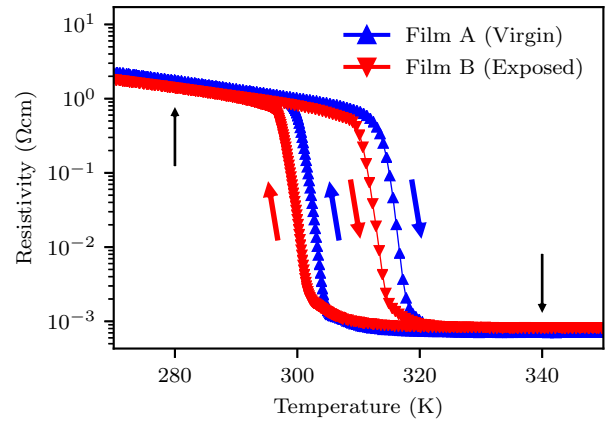

FIG. 3. Four-probe resistivity results for a virgin VO$_2$ film (film A, shown in blue) and for another film from the same batch after the ARPES experiment (film B, shown in red). The black arrows show the acquisition temperature for the ARPES data. Red and blue arrows indicate the scan direction of time during the measurements.

which is well below and above the MIT, as seen in Fig. 3. A Fermi-Dirac distribution, convoluted with a Gaussian and multiplied with a linear background, was fitted to the energy distribution curves (EDCs) in the metallic phase in order to determine the Fermi energy. The Fermi level determined in this way was used as a reference for the insulating phase. The geometric coordinates (θ, E_{ph}, E_{kin}) were mapped onto ($k_\parallel$, $k_\perp$, E_{bin}), assuming a free-electron final state of the photoemitted electron with an inner potential of $V_0 = 7$ eV and an effective mass m_e^* of $m_e^* = m_e$, where m_e is the electron rest mass. The inner potential and effective mass were chosen in order to obtain the best fit between the dispersion and lattice periodicity, and the present values were found to provide a better fit than $V_0 = 16$ eV used in previous studies [13,15].

III. COMPUTATIONAL DETAILS

The DFT calculations are carried out using the QUANTUM ESPRESSO [43] package, which uses a plane-wave basis set. The plane-wave cutoff for the DFT calculation was set at 250 Ry for the plane-wave expansion of the wave functions. Our calculation uses scalar-relativistic optimized norm-conserving Vanderbilt pseudopotentials (ONCVPSPs) [44] obtained from the PSEUDODOJO project [45]. The local-spin-density approximation (LSDA) was used for the DFT exchange-correlation functional. Hubbard-U correction [46–48] was applied within a simplified rotationally invariant formulation [49], using the Löwdin-orthogonalized atomic 3d pseudo wave functions of the V atoms as the localized basis set for the Hubbard manifold.

For the nonmagnetic metallic rutile phase, no Hubbard-U correction was made. In Fig. 6, we see that setting $U = 0.0$ eV [Fig. 6(a)] and $U = 2.0$ eV [Fig. 6(d)] for this phase resulted in only very minor changes to the band structure. For the antiferromagnetic insulating monoclinic phase, Hubbard-U correction of $U = 2.0$ eV was used, with each dimer being an antiferromagnetically coupled pair. The magnitude of U was set to reproduce the energy level of the topmost experimental V valence band. Further increasing U (to, e.g., 5.0 eV) does
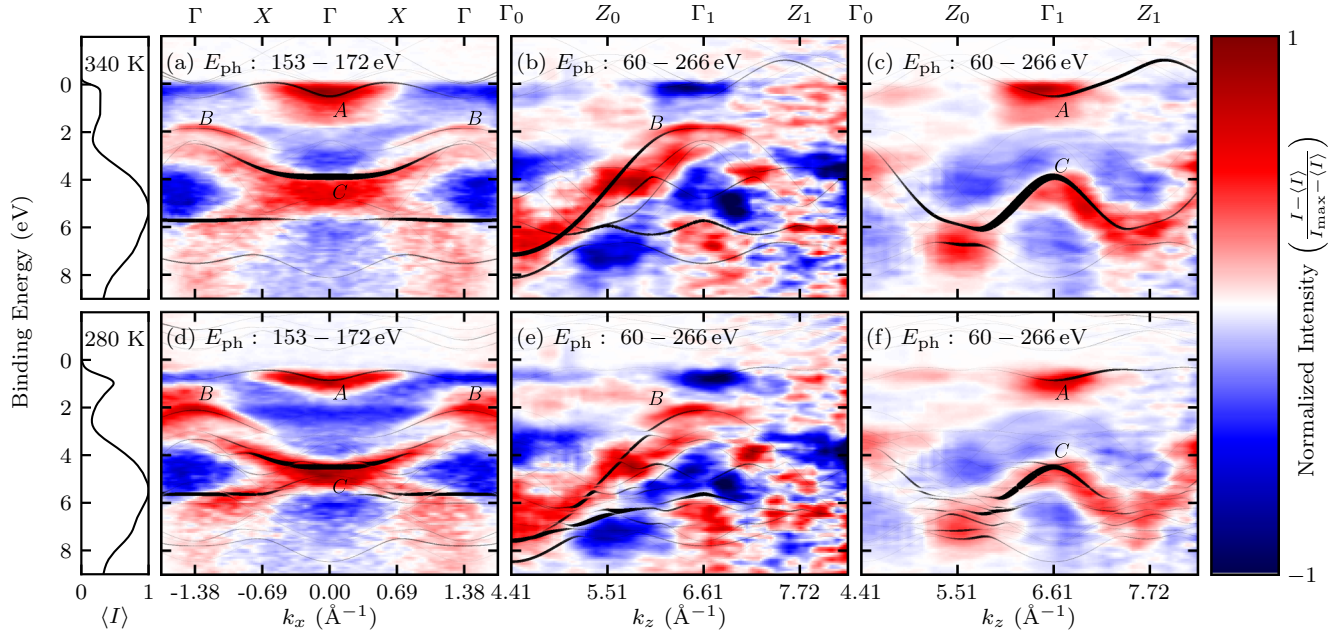
FIG. 4. ARPES data from a 20-nm-thick VO$_2$ film grown on TiO$_2$ substrates. The data were collected at (a)–(c) 340 K and (d)–(f) 280 K and averaged over $k_z = \pm 4\sigma_z$ with Gaussian weights using $\sigma_z = 60$ mÅ^{-1} centered at $k_z = 6.45$ Å^{-1} for (a) and (d), which is slightly off Γ. (b) and (e) and (c) and (f) show data averaged using $\sigma_x = 30$ mÅ^{-1} around $k_x = -1.38$ Å^{-1} and $k_x = 0.00$ Å^{-1} (i.e., at normal emission), respectively. Each energy distribution curve in the original data matrix has been shifted to zero mean intensity above the Fermi level and normalized to have equal integrated intensity. An inner potential of $V_0 = 7$ eV and the free-electron mass was used for the energy to momentum conversion prior to computing the k_x integrated spectral intensity $\langle I \rangle$, seen to the left. This intensity map was subtracted from the data to emphasize dispersing features. Calculated band structures unfolded in the extended-zone scheme for the rutile (R) and monoclinic (M_1) phases, respectively, are superimposed as black lines for comparison. The thickness and opacity of the lines are proportional to the square of the plane-wave components of the Bloch crystal wave functions as defined in Eq. (1). The calculated Kohn-Sham eigenenergies of the oxygen bands are rigidly shifted downwards by 0.19 and 1.0 eV for the rutile and monoclinic phases, respectively, as explained in Sec. III.

not change the nature of the band gap for both phases: the rutile phase remains metallic [Figs. 6(a), 6(d), and 6(g)], while the monoclinic phase remains insulating [Figs. 6(c), 6(f), and 6(i)]. To make up for the lack of quasiparticle self-energy corrections beyond the DFT approach, e.g., the *GW* correction [50,51], the Kohn-Sham eigenenergies of the calculated oxygen bands in Figs. 4 and 5 were rigidly shifted downwards by 0.19 and 1.0 eV for the rutile and monoclinic phases, respectively, to fit feature B in the experiment. As expected, the quasiparticle self-energy correction, such as within the *GW* approximation, lowers the valence Kohn-Sham band energies and is larger for insulators than metals [51].

In the experiment, ARPES measures the nonperiodic true momenta $\hbar k$ of a free electron that has left the crystal potential. In the DFT calculation, the calculated Bloch wave functions $\psi_{nk}(\mathbf{r})$ are Kohn-Sham eigenstates of the crystal Hamiltonian labeled by the crystal momenta $\hbar K$, which is periodic over different Brillouin zones. A Bloch wave function of a particular band index n and crystal momentum K is a superposition of free-electron plane waves $e^{ik \cdot \mathbf{r}}$ of different true momenta $\hbar k$. Hence, the experimental ARPES spectral intensity is better represented by the probability that the Bloch crystal wave function has the true momentum $\hbar k$ of a free electron, or, in other words, the square of the plane-wave components of the Bloch crystal wave function, namely,

$$P_{k,K} = |\langle e^{ik \cdot \mathbf{r}} | \psi_{nK}(\mathbf{r}) \rangle|^2. \quad (1)$$

By projecting the periodic Bloch wave functions onto plane waves, we unfold the Bloch wave function using an extended-zone scheme. The resulting unfolded band structure now incorporates the structure factor explicitly [52], thus facilitating a direct comparison with the ARPES experiments. Finally, we superimpose the experimental ARPES spectra onto the calculated band structures as weighted by $P_{k,K}$ that is defined in Eq. (1).

IV. RESULTS

Figure 3 shows resistivity curves from a freshly grown thin-film VO$_2$ sample (blue triangles) alongside the film used in the photoelectron experiment postmeasurement (red triangles). The data show that the change in transition temperature between a virgin film and an exposed film is 3 K, which is within the variation observed between samples analyzed immediately after deposition. In addition, the magnitude of the resistivity jump and the width of the hysteresis across the MIT are preserved, which strongly suggests that the film quality has remained the same during the ARPES experiment. Half-step values pinpoint T_c of the fresh sample to 303 and 316 K for falling and rising T, respectively. To make sure that the ARPES data were collected in the insulating and metallic phases the temperatures used were 280 and 340 K, respectively.
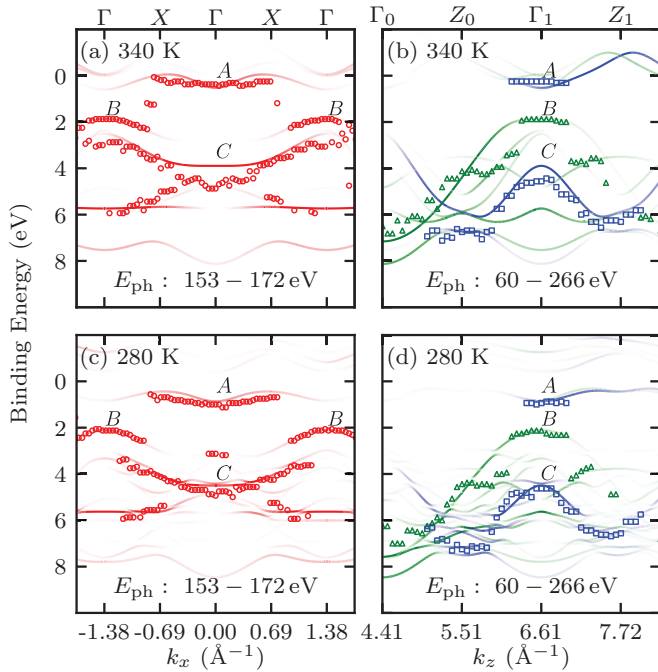
FIG. 5. Local intensity maxima from the data in Fig. 4 for which k_z-dispersive data from two different BZs are overlaid. Red circles in (a) and (c) are data taken from the ARPES map shown in Figs. 4(a) and 4(d), respectively. Data in (b) and (d) originate from scans shown in Figs. 4(b) and 4(c) and 4(e) and 4(f), where green triangles and blue squares are from $k_x = -1.38$ Å^{-1} and $k_x = 0$, respectively. Calculated bands from Fig. 4, with opacity proportional to $P_{k,K}$ and unfolded in the extended-zone scheme, are overlaid on top of the experimental data.

ARPES maps were measured from $hv = 153$ to 172 eV in search of k_x-dispersive features on the line $k_z = \frac{6\pi}{c}$ [see Figs. 4(a) and 4(d)]. A less detailed but wider scan from $hv = 60$ to 266 eV was performed to capture electron bands dispersing in the k_z direction [see Figs. 4(b), 4(c), 4(e), and 4(f)]. Both k_x and k_z cuts were measured above and below T_c. At both temperatures, angle integrated spectra $\langle I \rangle$ were obtained, for which the one at $k_z = \frac{6\pi}{c}$ is shown to the left of the ARPES maps in Fig. 4. For each k_z, the corresponding $\langle I \rangle$ was subtracted from the data to enhance dispersive features, which produced the final intensity difference shown in Figs. 4(a)–4(f).

The ARPES maps reveal several prominent features, three of which are labeled A to C and discussed in the following. At $T = 340$ K, a substantial intensity enhancement (A) is observed at the centered Γ (i.e., at normal emission for which $k_x = 0$). Through comparison to DFT calculations it can be assigned to V $3d$ orbitals that reach a maximum at $E_{bin} = 0.4$ eV [see Fig. 4(a)]. Matrix element effects result in substantial intensity variations between adjacent BZs, as seen, for example, with feature A, which is strongly suppressed off normal emission. Conversely, some features not seen at normal emission (i.e., $k_x = 0$) are observed off normal emission. The projected band structures calculated using DFT reproduce these effects quite well, as can be seen from the black lines overlaid on the ARPES measurements in Figs. 4(a)–4(f). A particularly noteworthy feature of our data is that they provide

evidence of a dispersive O $2p$ band in the binding energy region from 1.8 to 2.5 eV [see feature B in Figs. 4(a) and 4(b)]. Its full width at half maximum was determined to 0.33 ± 0.05 eV from Voigtian + linear background fits on normalized EDC curves. Another feature (C) of O $2p$ character is observed close to the centered Γ around 4.6 eV below the Fermi level, with a width of 1.3 eV. The large width indicates that the feature includes intensity contributions from additional bands. The difference between data at $k_x = -1.38$ Å^{-1} and normal emission is further clarified in Figs. 4(b) and 4(c), respectively. Feature B clearly disperses in the Γ-Z direction, which is captured by theory and shown in Fig. 4(b). In Fig. 4(c) the spectral weight is shifted in favor of the feature denoted C, which is clearly captured by the calculations. From Figs. 4(b) and 4(c) it becomes clear that the spectral weight for features A and C is strongest at normal emission, while feature B becomes emphasized in the adjacent BZs.

The data shown in Figs. 4(d)–4(f) reveal a similar data set taken at $T = 280$ K $< T_c$. Most notably, a pronounced gap opens up at the Fermi level, shifting the valence band edge by approximately 0.3 eV. This is consistent with the insulating nature of the low-temperature phase and in agreement with earlier observations [53]. The opening of the insulating gap shifts the V $3d$ band to approximately $E_{bin} = 1.0$ eV. Similarly, feature B is pushed 0.24 eV towards higher binding energies. It is recognized that the width of feature B increases by 30% to 0.4 ± 0.1 eV. In contrast, feature C sharpens by almost 0.4 eV, possibly indicating a narrower band coincidence. Apart from the gap opening at the Fermi level, the data in Figs. 4(e) and 4(f) change only slightly compared to those in the metallic phase. The most notable change concerns the curvature of feature B. It is shifted approximately 0.2 eV to higher binding energies, while the signature of feature C resembles the behavior in the insulating phase.

By extracting experimental binding energies of the maximal spectral intensities in Figs. 4(a)–4(f), one can compare the experimental data with the calculated binding energies. In Figs. 5(a)–5(d), we compare the band positions of features A–C. To give a more complete picture, the k_z-dispersive data from two different BZs from Figs. 4(b) and 4(c) are overlaid in Fig. 5(b). Similarly, Figs. 4(e) and 4(f) are overlaid in Fig. 5(d). Most notably, there are very good agreements between experiment and theory for features B and C of the corresponding bands for both phases. Effective masses (m_x^*, m_z^*) for feature B were determined to $(-2.1 \pm 0.2, -3.2 \pm 0.5)m_e$ for the rutile phase and $(-1.4 \pm 0.1, -3.6 \pm 1.2)m_e$ for the insulating phase. This result compares well to theory, for which the corresponding masses are $(-2.09 \pm 0.02, -3.4 \pm 0.07)m_e$ and $(-1.52 \pm 0.006, -1.71 \pm 0.005)m_e$ for the rutile and monoclinic calculations, respectively. Further details on the calculated band structure, extracted band positions, and band masses can be found in the Appendices A and B.

V. DISCUSSION

Our results demonstrate very good agreement between theory and experiment, as shown in Figs. 4 and 5. In particular, we see excellent agreement in the spectral intensities of the O bands, which have broad dispersions. In Fig. 4, strong experimental spectral intensities (represented by red in the

two-dimensional plots) are measured with a broad dispersion spanning binding energies between ~2 and ~8 eV. The calculated spectral intensities (represented by black lines of corresponding thickness and opacity) reproduce these dispersions very well. On the other hand, minor discrepancies between theory and experiment occur whenever the calculated bands are relatively flat. For example, the calculated intensities are strong for E_{bin} of around 5.9 ± 0.4 eV at $k_x = \pm 1.7$ Å^{-1} in Figs. 4(a) and 4(b) and $k_z = 5.9$ Å^{-1} in Figs. 4(d) and 4(e), whereas the corresponding experimental spectral intensities are weak. This observation is interesting but expected because unlike the bands with large dispersions, which have dominating O characters, these flat bands have strongly hybridized O and V characters. When the Bloch wave functions of these bands are projected onto the V atomic pseudowave function, the square of the projection is approximately 50%. This dispersion-free band is localized in real space and exhibits most features of a DFT or DFT+U electronic structure that indicates a strongly correlated electronic state. The discrepancy between theory and experiment could therefore be a reflection that the multiconfigurational nature of such a strongly correlated state cannot be completely captured using a single-Slater-determinant approach and requires the use of a more advanced theory like the dynamical mean-field theory (DMFT). That, however, is beyond the scope of the present investigation.

Technically, the theoretical approach used here is computationally much more efficient but is also a significantly less accurate description of the V 3d electrons of the monoclinic phase, compared, for instance, to the treatment in Ref. [54]. In that work, a cluster approach of DMFT was employed to describe the correlated electronic structure of monoclinic VO$_2$, such that the V 3d manifold was argued to form a multiconfigurational singlet state. It is interesting that a significantly simpler treatment as employed here based on a single-Slater-determinant description reproduces the measured band dispersion with good accuracy.

Turning now to the experimental results, in the insulating phase the leading edge of the upper V band is pushed 0.3 eV below the Fermi edge. Assuming a Fermi level centered in the gap, our results indicate a gap of ~0.6 eV, which is close to the optical band gap of bulk VO$_2$, which is 0.7 eV [55]. This result is in agreement with reported cluster DMFT calculations [56] and earlier photoelectron results [57], interpreting the transition in view of a dimerization picture in which concurrent correlation effects lift the π^* states above the Fermi level and split the $d_{\parallel}$ states into two Hubbard bands. However, in contrast to these results we also find a strong engagement of the O 2p bands in the MIT, as an almost rigid shift of the entire band structure by approximately 300 meV is observed. The shift decreases from the Fermi level and towards higher binding energy, leading to an overall compression of the valence band.

We end this section with an analysis of the conditions necessary for the current theoretical model to display an MIT between the rutile and monoclinic phase. As shown in Fig. 6, within the theoretical model employed here, the insulating phase of VO$_2$ needs both the correct crystal structure (monoclinic and not rutile) as well as a Hubbard U to be stabilized. If only the correct structure (i.e., a monoclinic structure with

$U = 0.0$ eV) were needed to stabilize the gap, such an MIT would properly be described as a pure Peierls (or Jones) transition. However, the calculated band structure of such a system is metallic [Fig. 6(c)]. On the other hand, if only Hubbard U were needed to stabilize the gap, it would be described as a pure Mott transition. This is expected to be independent of the crystal structure, so that as a function of increasing U, a gap would open in a similar way for the monoclinic phase and the nonmagnetic or antiferromagnetic rutile structure. However, the calculated band structure of the nonmagnetic rutile phase is metallic for all choices of U considered here [Figs. 6(a), 6(d), and 6(g)], and for the antiferromagnetic rutile structure (in which the two V atoms forming the unit cell are antiferromagnetically coupled), it is metallic up to U of ~3.8 eV [Figs. 6(b) and 6(e)]. For U larger than 3.8 eV, an antiferromagnetic rutile structure would be insulating [Fig. 6(h)], but the topmost V 3d band would also be pushed downwards to become entangled with the O manifold. This is contrary to the experimental ARPES observation in Fig. 4, which shows that the topmost V band is isolated from the O manifold, indicating that $U > 3.8$ eV is unrealistic. VO$_2$ is therefore a rather unique case in which both the Peierls (or Jones) transition and Hubbard U are needed to give a MIT at a physically reasonable place in the parameter space. Therefore, it would be appropriate to describe the MIT as a Mott+Peierls (or Mott+Jones) transition.

VI. SUMMARY

The metal-to-insulator transition of VO$_2$ has been revisited using angle-resolved photoelectron spectroscopy. Data from the two phases were collected, thus permitting a direct comparison of the experimentally determined electronic structure in the two phases. The results demonstrate a substantial shift of the band energy deep down into the valence bands, while only minor changes in the energy dispersion are observed. The experimental results were compared to electronic structure calculations, and very good agreement was found between the experimental results and calculations when an explicit Hubbard U is included for the insulating phase. The existence of a large collective shift and valence band compression, together with good agreement with theoretical results, support the picture of the insulating phase as a Mott-Hubbard insulator and underline the importance of correlation effects in the metal-to-insulator transition.
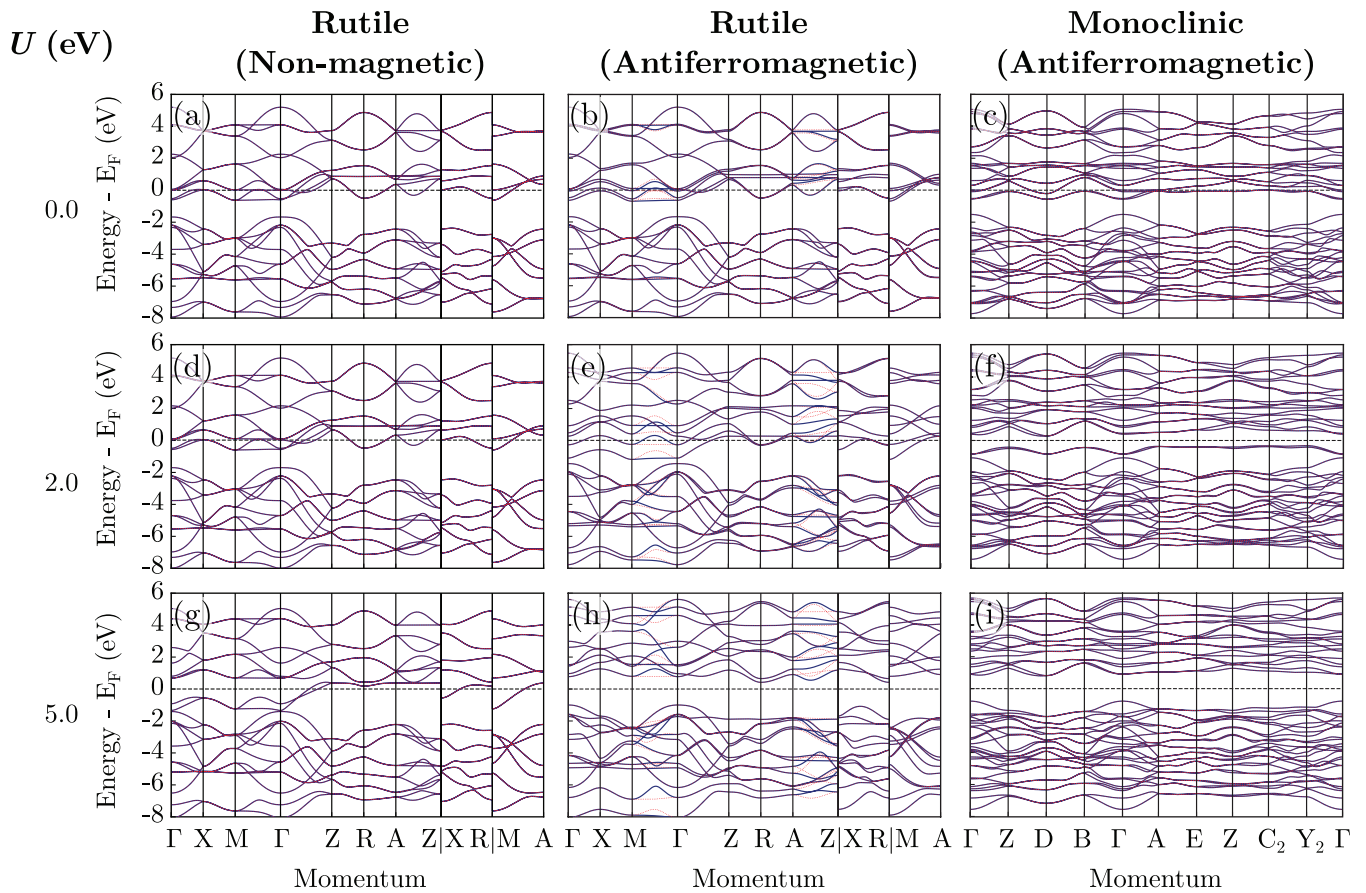
FIG. 6. Calculated spin-polarized LSDA+U band structures. Solid blue line are bands for spin-up electrons, while dotted red lines are for spin-down electrons. E_F denotes the Fermi level. (a), (d), and (g) are the calculated band structures with $U = 0.0$, 2.0, 5.0 eV, respectively, for the nonmagnetic rutile phase, while (c), (f), and (i) are those for the antiferromagnetic monoclinic phase, in which each dimer forms an antiferromagnetic pair. (b), (e), and (h) are the calculated band structures of a hypothetical system which has a rutile structure, in which the two V atoms forming the unit cell are antiferromagnetically coupled with $U = 0.0$, 2.0, 5.0 eV, respectively.

APPENDIX A: DFT BAND STRUCTURE CALCULATIONS

In Fig. 6, we plot the calculated DFT band structure within the spin-polarized LSDA+U approximation along
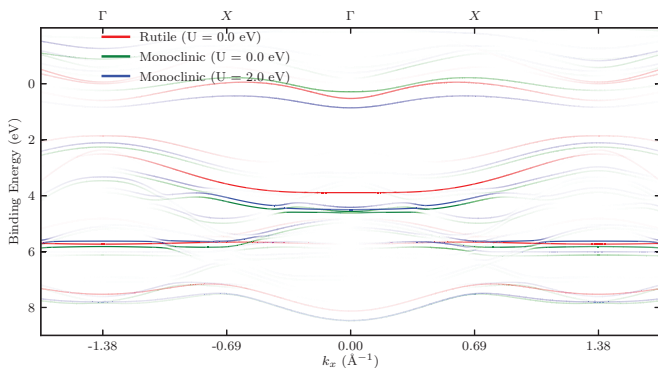

FIG. 7. Calculated spin-polarized LSDA+U band structures along the Γ-X direction for the nonmagnetic rutile phase for $U = 0.0$ eV [red, Fig. 4(a)] and the antiferromagnetic monoclinic phase for $U = 0.0$ eV (green) and 2.0 eV [blue, Fig. 4(d)]. The opacity of the bands is proportional to the projection of these calculated Bloch bands onto free-electron final states, as described in Sec. III. As in Figs. 4 and 5, the bands have been shifted to fit experimental data.
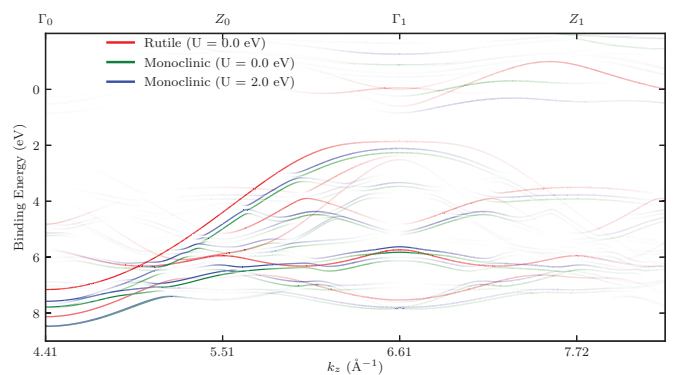

FIG. 8. Band structure plot similar to Fig. 7, but along the Γ-Z direction at $k_x = -1.37$ Å^{-1} for the nonmagnetic rutile phase for $U = 0.0$ eV [red, Fig. 4(b)] and the antiferromagnetic monoclinic phase for $U = 0.0$ eV (green) and 2.0 eV [blue, Fig. 4(e)].

FIG. 9. Band structure plot similar to Fig. 7, but along the Γ-Z direction at normal emission (i.e., $k_x = 0.00$ Å^{-1}) for the nonmagnetic rutile phase for $U = 0.0$ eV [red, Fig. 4(c)] and the antiferromagnetic monoclinic phase for $U = 0.0$ eV (green) and 2.0 eV [blue, Fig. 4(f)].
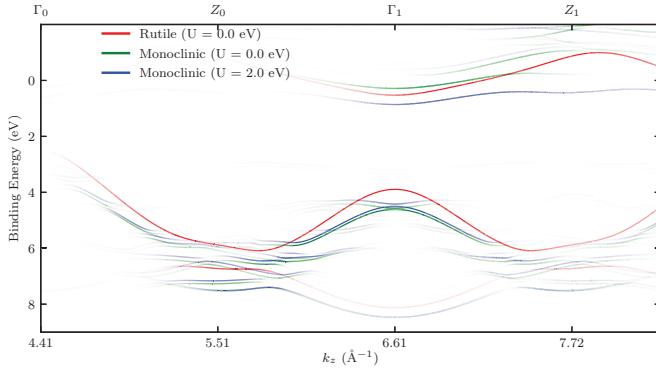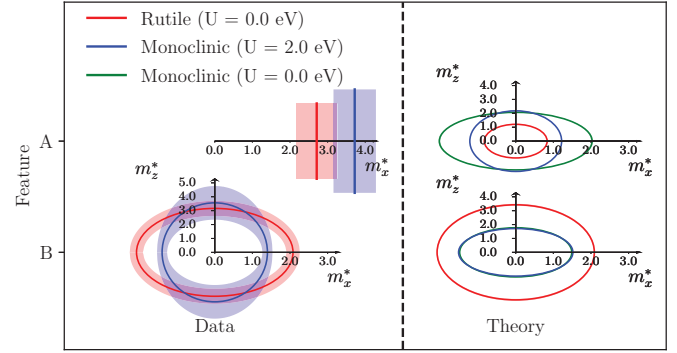

FIG. 10. Illustration of the effective masses for features A and B using data taken from Table II. The center line represents the estimated value, with the error given by the lighter region behind it. The equation for the ellipses is $(x/m_x^*)^2 + (z/m_z^*)^2 = 1$ in the three plots where both projections could be estimated.

k paths [58] in the reciprocal space. For both the nonmagnetic metallic rutile phase and the antiferromagnetic insulating monoclinic phase, Hubbard-U corrections of $U = 0.0, 2.0, 5.0$ eV were used. The nature of the band gap for both phases does not change when U is increased from $U = 0.0$ eV to $U = 5.0$ eV; that is, the rutile phase remains metallic [Figs. 6(a), 6(d), and 6(g)], while the monoclinic phase remains insulating [Figs. 6(c), 6(f), and 6(i)]. We also considered the hypothetical case in which the two V atoms in the rutile unit cell are antiferromagnetically coupled. We found that such a hypothetical structure is metallic up to U of $\sim$3.8 eV [Figs. 6(d) and 6(e)]. For U larger than 3.8 eV, an antiferromagnetic rutile structure would be insulating [Fig. 6(f)], but the topmost V $3d$ band would also be pushed downwards to become entangled with the O manifold, making it unrealistic (see discussion in main text).

In Figs. 7–9, we show the calculated DFT band structures along **k** paths corresponding to the three columns in Fig. 4 from left to right, respectively.

APPENDIX B: EXTRACTION OF PARAMETERS

Band positions and effective masses were determined by fitting a second-degree polynomial around the high-symmetry points of chosen bands in the range $|k_x - k_0| < 0.2$ Å^{-1}. The coefficient c in front of the k^2 for the best-fit parabola can then be used to estimate the effective mass through $m^*/m_e = -3.81/c$ if c is written in Ångström. To be consistent, the same estimate was used for the calculations even though a more exact method could be used in some cases. For instance, using a higher degree polynomial and extracting the coefficient in front of the second-order term is more correct but is more prone to numerical instability. The errors are taken to be $\sigma_k = \sqrt{C_{kk}}$, where C_{ij} is the parameter covariance matrix from the fitting procedure. All extracted parameters are displayed in Table II where the effective masses of feature A and B are illustrated in Fig. 10.

TABLE II. Estimated dispersion parameters from experimental data compared to theory. A dash (—) means that no value could be determined. R stands for rutile with $U = 0.0$ eV, M stands for monoclinic (M_1) with $U = 2.0$ eV, and N stands for monoclinic (M_1) with $U = 0.0$ eV. The binding energy of oxygen bands has been shifted by 0.19 and 1.0 eV for the rutile and monoclinic calculations, respectively (as in Fig. 7).

Feature	Phase	Projection	Source	k_x (Å^{-1})	E_{bin}^0 (eV)	m^*/m_e
A	R	X	Theory	0	$3.91 \times 10^{-1} \pm 9.62 \times 10^{-3}$	$+2.71 \times 10^{+0} \pm 5.51 \times 10^{-1}$
A	R	Z	Data	0	$5.28 \times 10^{-1} \pm 5.66 \times 10^{-5}$	$+1.21 \times 10^{+0} \pm 3.65 \times 10^{-3}$
A	R	Z	Theory	0	$2.66 \times 10^{-1} \pm 2.71 \times 10^{-2}$	—
A	N	X	Data	0	$2.88 \times 10^{-1} \pm 2.38 \times 10^{-4}$	$+2.03 \times 10^{+0} \pm 2.60 \times 10^{-2}$
A	N	Z	Theory	0	$2.86 \times 10^{-1} \pm 1.87 \times 10^{-4}$	$+2.07 \times 10^{+0} \pm 1.12 \times 10^{-2}$
A	M	X	Theory	0	$8.61 \times 10^{-1} \pm 2.30 \times 10^{-5}$	$+1.22 \times 10^{+0} \pm 1.16 \times 10^{-3}$
A	M	X	Theory	0	$1.01 \times 10^{+0} \pm 1.52 \times 10^{-2}$	$+3.72 \times 10^{+0} \pm 5.64 \times 10^{-1}$
A	M	Z	Data	0	$8.55 \times 10^{-1} \pm 9.66 \times 10^{-4}$	$+2.18 \times 10^{+0} \pm 2.16 \times 10^{-2}$
A	M	Z	Theory	0	$9.28 \times 10^{-1} \pm 2.06 \times 10^{-2}$	—
A	R	X	Data	0	$5.15 \times 10^{-1} \pm 1.76 \times 10^{-3}$	$+8.35 \times 10^{-1} \pm 9.96 \times 10^{-3}$

TABLE II. (*Continued.*)

Feature	Phase	Projection	Source	k_x (Å^{-1})	E_{bin}^0 (eV)	m^*/m_e
B	*R*	*X*	Data	−1.38	$1.86 \times 10^{+0} \pm 7.39 \times 10^{-4}$	$-2.09 \times 10^{+0} \pm 1.98 \times 10^{-2}$
B	*R*	*X*	Theory	−1.38	$1.86 \times 10^{+0} \pm 6.63 \times 10^{-3}$	$-2.08 \times 10^{+0} \pm 1.80 \times 10^{-1}$
B	*R*	*X*	Data	1.38	$1.85 \times 10^{+0} \pm 6.34 \times 10^{-4}$	$-2.01 \times 10^{+0} \pm 7.88 \times 10^{-3}$
B	*R*	*X*	Theory	1.38	$1.90 \times 10^{+0} \pm 1.46 \times 10^{-2}$	$-2.22 \times 10^{+0} \pm 2.24 \times 10^{-1}$
B	*R*	*Z*	Data	−1.38	$1.85 \times 10^{+0} \pm 2.31 \times 10^{-3}$	$-3.42 \times 10^{+0} \pm 7.20 \times 10^{-2}$
B	*R*	*Z*	Theory	−1.38	$1.86 \times 10^{+0} \pm 1.14 \times 10^{-2}$	$-3.16 \times 10^{+0} \pm 5.43 \times 10^{-1}$
B	*N*	*X*	Data	−1.38	$2.26 \times 10^{+0} \pm 2.54 \times 10^{-4}$	$-1.49 \times 10^{+0} \pm 3.13 \times 10^{-3}$
B	*N*	*Z*	Theory	−1.38	$2.26 \times 10^{+0} \pm 4.34 \times 10^{-4}$	$-1.77 \times 10^{+0} \pm 5.86 \times 10^{-3}$
B	*M*	*X*	Theory	1.38	$2.11 \times 10^{+0} \pm 4.50 \times 10^{-4}$	$-1.47 \times 10^{+0} \pm 4.42 \times 10^{-3}$
B	*M*	*X*	Theory	1.38	$2.08 \times 10^{+0} \pm 1.20 \times 10^{-2}$	$-1.37 \times 10^{+0} \pm 8.07 \times 10^{-2}$
B	*M*	*X*	Theory	−1.38	$2.21 \times 10^{+0} \pm 7.28 \times 10^{-4}$	$-1.52 \times 10^{+0} \pm 6.30 \times 10^{-3}$
B	*M*	*X*	Data	−1.38	$2.10 \times 10^{+0} \pm 1.79 \times 10^{-2}$	$-1.40 \times 10^{+0} \pm 1.35 \times 10^{-1}$
B	*M*	*Z*	Theory	−1.38	$2.10 \times 10^{+0} \pm 6.51 \times 10^{-4}$	$-1.71 \times 10^{+0} \pm 5.20 \times 10^{-3}$
B	*M*	*Z*	Data	−1.38	$2.18 \times 10^{+0} \pm 2.83 \times 10^{-2}$	$-3.56 \times 10^{+0} \pm 1.21 \times 10^{+0}$
C	*R*	*X*	Theory	0	$3.90 \times 10^{+0} \pm 4.26 \times 10^{-4}$	$+1.81 \times 10^{+1} \pm 5.81 \times 10^{-1}$
C	*R*	*X*	Data	0	$4.70 \times 10^{+0} \pm 3.36 \times 10^{-2}$	$+1.96 \times 10^{+0} \pm 1.12 \times 10^{-1}$
C	*R*	*Z*	Theory	0	$3.90 \times 10^{+0} \pm 1.03 \times 10^{-3}$	$-5.00 \times 10^{-1} \pm 2.55 \times 10^{-3}$
C	*R*	*Z*	Data	0	$4.55 \times 10^{+0} \pm 5.45 \times 10^{-2}$	$-1.07 \times 10^{+0} \pm 1.38 \times 10^{-1}$
C	*N*	*X*	Theory	0	$4.61 \times 10^{+0} \pm 6.43 \times 10^{-4}$	$+1.13 \times 10^{+1} \pm 7.33 \times 10^{-1}$
C	*N*	*X*	Theory	0	$4.62 \times 10^{+0} \pm 5.92 \times 10^{-4}$	$-6.29 \times 10^{-1} \pm 2.97 \times 10^{-3}$
C	*M*	*X*	Theory	0	$4.50 \times 10^{+0} \pm 7.59 \times 10^{-5}$	$+1.05 \times 10^{+1} \pm 8.57 \times 10^{-2}$
C	*M*	*X*	Data	0	$4.79 \times 10^{+0} \pm 2.22 \times 10^{-2}$	$+2.85 \times 10^{+0} \pm 1.70 \times 10^{-1}$
C	*M*	*Z*	Theory	0	$4.50 \times 10^{+0} \pm 4.38 \times 10^{-4}$	$-5.56 \times 10^{-1} \pm 4.47 \times 10^{-3}$
C	*M*	*Z*	Data	0	$4.71 \times 10^{+0} \pm 9.99 \times 10^{-2}$	$-1.16 \times 10^{+0} \pm 2.97 \times 10^{-1}$

[1] A. Mansingha, R. Singh, and S. B. Krupanidhi, Electrical switching in single crystal VO$_2$, Solid-State Electron. **23**, 649 (1980).

[2] M. Pattanayak, M. N. F. Hoque, Z. Fan, and A. A. Bernussi, Electrical oscillation generation with current-induced resistivity switching in VO$_2$ micro-channel devices, Science Technol. Adv. Mater. **19**, 693 (2018).

[3] F. J. Morin, Oxides Which Show a Metal-to-Metal Transition at the Neel Temperature, Phys. Rev. Lett. **3**, 34 (1959).

[4] A. Cavalleri, C. Tóth, C. W. Siders, J. A. Squier, F. Ráksi, P. Forget, and J. C. Kieffer, Femtosecond Structural Dynamics in VO$_2$ during an Ultrafast Solid-Solid Phase Transition, Phys. Rev. Lett. **87**, 237401 (2001).

[5] P. Baum, D.-S. Yang, and A. H. Zewail, 4D visualization of transitional structures in phase transformations by electron diffraction, Science **318**, 788 (2007).

[6] V. A. Lobastov, J. Weissenrieder, J. Tang, and A. H. Zewail, Ultrafast electron microscopy (UEM): Four-dimensional imaging and diffraction of nanostructures during phase transitions, Nano Lett. **7**, 2552 (2007).

[7] K. M. Martens, I. P. Radu, G. Rampelberg, J. Verbruggen, S. Cosemans, S. Mertens, X. Shi, M. Schaekers, C. Huyghebaert, S. De-Gendt, C. Detavernier, M. Heyns, and J. A. Kittl, VO$_2$, a metal-insulator transition material for nanoelectronic applications, ECS Trans. **45**, 151 (2012).

[8] V. R. Morrison, R. P. Chatelain, K. L. Tiwari, A. Hendaoui, A. Bruhács, M. Chaker, and B. J. Siwick, A photoinduced metal-like phase of monoclinic VO$_2$ revealed by ultrafast electron diffraction, Science **346**, 445 (2014).

[9] S. Wall, S. Yang, L. Vidas, M. Chollet, J. M. Glownia, M. Kozina, T. Katayama, T. Henighan, M. Jiang, T. A. Miller, D. A. Reis, L. A. Boatner, O. Delaire, and M. Trigo, Ultrafast disordering of vanadium dimers in photoexcited VO$_2$, Science **362**, 572 (2018).

[10] M. M. Qazilbash, M. Brehm, B.-G. Chae, P.-C. Ho, G. O. Andreev, B.-J. Kim, S. J. Yun, A. V. Balatsky, M. B. Maple, F. Keilmann, H.-T. Kim, and D. N. Basov, Mott transition in VO$_2$ revealed by infrared spectroscopy and nano-imaging, Science **318**, 1750 (2007).

[11] J. H. Park, J. M. Coy, T. S. Kasirga, C. Huang, Z. Fei, S. Hunter, and D. H. Cobden, Measurement of a solid-state triple point at the metal–insulator transition in VO$_2$, Nature (London) **500**, 431 (2013).

[12] W. H. Brito, M. C. O. Aguiar, K. Haule, and G. Kotliar, Metal-Insulator Transition in VO$_2$: A DFT + DMFT Perspective, Phys. Rev. Lett. **117**, 056402 (2016).

[13] K. Saeki, T. Wakita, Y. Muraoka, M. Hirai, T. Yokoya, R. Eguchi, and S. Shin, Band dispersion near the Fermi level for VO$_2$ thin films grown on TiO$_2$ (001) substrates, Phys. Rev. B **80**, 125406 (2009).

[14] L. Moreschini, Y. J. Chang, D. Innocent, A. L. Walter, Y. S. Kim, G. Gaines, A. Bostwick, J. Denlinger, and E. Rotenberg, Bull. Am. Phys. Soc. (D22.00001) March Meeting, Dallas, 2012, http://meetings.aps.org/link/BAPS.2011.MAR.D22.1.

[15] Y. Muraoka, H. Nagao, Y. Yao, T. Wakita, K. Terashima, T. Yokoya, H. Kumigashira, and M. Oshima, Fermi surface topology in a metallic phase of VO$_2$ thin films grown on TiO$_2$(001) substrates, Sci. Rep. **8**, 17906 (2018).

[16] A. Shigemoto, S. Suga, A. Sekiyama, S. Imada, A. Yamasaki, A. Irizawa, S. Kasai, T. Muro, Y. Saitoh, Y. Ueda, and K. Yoshimurae, Bulk sensitive photoemission studies of metal-insulator transition in V_6O_{13} and VO_2, J. Electron. Spectrosc. **144–147**, 837 (2005).

[17] J. B. Goodenough, The two components of the crystallographic transition in VO_2, J. Solid State Chem. **3**, 490 (1971).

[18] J. B. Goodenough, Metallic oxides, Prog. Solid State Chem. **5**, 145 (1971).

[19] H. Terauchi and J. B. Cohen, Diffuse x-ray scattering due to the lattice instability near the metal-semiconductor transition in VO_2, Phys. Rev. B **17**, 2494 (1978).

[20] D. Maurer, A. Leue, R. Heichele, and V. Müller, Elastic behavior near the metal-insulator transition of VO_2, Phys. Rev. B **60**, 13249 (1999).

[21] V. Eyert, The metal-insulator transition of VO_2: A band theoretical approach, Ann. Phys. (Berlin, Ger.) **11**, 650 (2002).

[22] V. Eyert, VO_2: A Novel View from Band Theory, Phys. Rev. Lett. **107**, 016401 (2011).

[23] S. Westman, Note on a phase transition in VO2, Acta Chem. Scand. **15**, 217 (1961).

[24] G. Andersson, Studies on vanadium oxides. II. The crystal structure of vanadium dioxide, Acta Chem. Scand. **10**, 623 (1956).

[25] M. Marezio, D. B. McWhan, J. P. Remeika, and P. D. Dernier, Structural aspects of the metal-insulator transitions in Cr-doped VO_2, Phys. Rev. B **5**, 2541 (1972).

[26] J. Galy and G. Miehe, Ab initio structures of (M2) and (M3) VO_2 high pressure phases, Solid State Sciences **1**, 433 (1999).

[27] Y. Oka, S. Sato, T. Yao, and N. Yamamoto, Crystal structures and transition mechanism of VO_2(A), J. Solid State Chem. **141**, 594 (1998).

[28] D. B. McWhan, M. Marezio, J. P. Remeika, and P. D. Dernier, X-ray diffraction study of metallic VO_2, Phys. Rev. B **10**, 490 (1974).

[29] H. Qiu, M. Yang, Y. Dong, H. Xu, B. Hong, Y. Gu, Y. Yang, C. Zou, Z. Luo, and C. Gao, The tetragonal-like to rutile structural phase transition in epitaxial VO_2/TiO_2(001) thick films, New J. Phys. **17**, 113016 (2015).

[30] Y. Zhang, L. Liu, and T. Y. Zhang, Strain relaxation in heteroepitaxial films by misfit twinning: II. equilibrium morphology, J. Appl. Phys. **101**, 063502 (2007).

[31] M. Yang, Y. Yang, B. Hong, L. Wang, K. Hu, Y. Dong, H. Xu, H. Huang, J. Zhao, H. Chen, L. Song, H. Ju, J. Zhu, J. Bao, X. Li, Y. Gu, T. Yang, X. Gao, Z. Luo, and C. Gao, Suppression of structural phase transition in VO_2 by epitaxial strain in vicinity of metal-insulator transition, Sci. Rep. **6**, 2045 (2016).

[32] A. X. Gray, J. Jeong, N. P. Aetukuri, P. Granitzka, Z. Chen, R. Kukreja, D. Higley, T. Chase, A. H. Reid, H. Ohldag, M. A. Marcus, A. Scholl, A. T. Young, A. Doran, C. A. Jenkins, P. Shafer, E. Arenholz, M. G. Samant, S. S. P. Parkin, and H. A. Dürr, Correlation-Driven Insulator-Metal Transition in Near-Ideal Vanadium Dioxide Films, Phys. Rev. Lett. **116**, 116403 (2016).

[33] D. Shiga, B. E. Yang, N. Hasegawa, T. Kanda, R. Tokunaga, K. Yoshimatsu, R. Yukawa, M. Kitamura, K. Horiba, and H. Kumigashira, Thickness dependence of electronic structures in Vo$_2$ ultrathin films: Suppression of the cooperative Mott-Peierls transition, Phys. Rev. B **102**, 115114 (2020).

[34] M. W. Haverkort, Z. Hu, A. Tanaka, W. Reichelt, S. V. Streltsov, M. A. Korotin, V. I. Anisimov, H. H. Hsieh, H.-J. Lin, C. T. Chen, D. I. Khomskii, and L. H. Tjeng, Orbital-Assisted Metal-Insulator Transition in VO_2, Phys. Rev. Lett. **95**, 196404 (2005).

[35] K. Okimura, T. Watanabe, and J. Sakai, Stress-induced VO_2 films with M_2 monoclinic phase stable at room temperature grown by inductively coupled plasma-assisted reactive sputtering, J. Appl. Phys. **111**, 073514 (2012).

[36] R. M. Wentzcovitch, W. W. Schulz, and P. B. Allen, VO_2: Peierls or Mott-Hubbard? A View from Band Theory, Phys. Rev. Lett. **72**, 3389 (1994).

[37] G. Stefanovich, A. Pergament, and D. Stefanovich, Electrical switching and Mott transition in VO_2, J. Phys.: Condens. Matter **12**, 8837 (2000).

[38] D. Lee, B. Chung, Y. Shi, G.-Y. Kim, N. Campbell, F. Xue, K. Song, S.-Y. Choi, J. P. Podkaminer, T. H. Kim, P. J. Ryan, J.-W. Kim, T. R. Paudel, J.-H. Kang, J. W. Spinuzzi, D. A. Tenne, E. Y. Tsymbal, M. S. Rzchowski, L. Q. Chen, J. Lee, and C. B. Eom, Isostructural metal-insulator transition in VO_2, Science **362**, 1037 (2018).

[39] Z. Shao, X. Cao, H. Luo, and P. Jin, Recent progress in the phase-transition mechanism and modulation of vanadium dioxide materials, npg Asia Mater. **10**, 581 (2018).

[40] F. Grandi, A. Amaricci, and M. Fabrizio, Unraveling the Mott-Peierls intrigue in vanadium dioxide, Phys. Rev. Research **2**, 013298 (2020).

[41] G. J. Paez, C. N. Singh, M. J. Wahila, K. E. Tirpak, N. F. Quackenbush, S. Sallis, H. Paik, Y. Liang, D. G. Schlom, T.-L. Lee, C. Schlueter, W.-C. Lee, and L. F. J. Piper, Simultaneous Structural and Electronic Transitions in Epitaxial VO_2/TiO_2(001), Phys. Rev. Lett. **124**, 196402 (2020).

[42] M. Muntwiler, J. Zhang, R. Stania, F. Matsui, P. Oberta, U. Flechsig, L. Patthey, C. Quitmann, T. Glatzel, R. Widmer, E. Meyer, T. A. Jung, P. Aebi, R. Fasel, and T. Greber, Surface science at the PEARL beamline of the Swiss Light Source, J. Synchrotron Radiat. **24**, 354 (2016).

[43] P. Giannozzi *et al.*, Quantum ESPRESSO: A modular and open-source software project for quantum simulations of materials, J. Phys. Condens. Matter **21**, 395502 (2009).

[44] D. R. Hamann, Optimized norm-conserving Vanderbilt pseudopotentials, Phys. Rev. B **88**, 085117 (2013).

[45] M. van Setten, M. Giantomassi, E. Bousquet, M. Verstraete, D. Hamann, X. Gonze, and G.-M. Rignanese, The pseudodojo: Training and grading a 85 element optimized norm-conserving pseudopotential table, Comput. Phys. Commun. **226**, 39 (2018); our V and O pseudopotentials are calculated using ONCVPSP version 0.4.1, as downloaded from http://www.pseudo-dojo.org/pseudos/nc-sr-04_pw_standard/V.upf.gz and http://www.pseudo-dojo.org/pseudos/nc-sr-04_pw_standard/V.upf.gz, respectively.

[46] V. I. Anisimov, J. Zaanen, and O. K. Andersen, Band theory and Mott insulators: Hubbard *U* instead of Stoner *I*, Phys. Rev. B **44**, 943 (1991).

[47] A. I. Anisimov, F. Aryasetiawan, and A. I. Lichtenstein, First-principles calculations of the electronic structure and spectra of strongly correlated systems: The LDA+U method, J. Phys.: Condens. Matter **9**, 767 (1997).

[48] S. L. Dudarev, G. A. Botton, S. Y. Savrasov, C. J. Humphreys, and A. P. Sutton, Electron-energy-loss spectra and the structural

stability of nickel oxide: An LSDA+U study, Phys. Rev. B **57**, 1505 (1998).

[49] M. Cococcioni and S. de Gironcoli, Linear response approach to the calculation of the effective interaction parameters in the LDA + U method, Phys. Rev. B **71**, 035105 (2005).

[50] M. S. Hybertsen and S. G. Louie, First-Principles Theory of Quasiparticles: Calculation of Band Gaps in Semiconductors and Insulators, Phys. Rev. Lett. **55**, 1418 (1985).

[51] M. S. Hybertsen and S. G. Louie, Electron correlation in semiconductors and insulators: Band gaps and quasiparticles energies, Phys. Rev. B **34**, 5390 (1986).

[52] W. Ku, T. Berlijn, and C. C. Lee, Unfolding First-Principles Band Structures, Phys. Rev. Lett. **104**, 216401 (2010).

[53] T. C. Koethe, Z. Hu, M. W. Haverkort, C. Schüßler-Langeheine, F. Venturini, N. B. Brookes, O. Tjernberg, W. Reichelt, H. H. Hsieh, H.-J. Lin, C. T. Chen, and L. H. Tjeng, Transfer of Spectral Weight and Symmetry across the Metal-Insulator Transition in VO_2, Phys. Rev. Lett. **97**, 116402 (2006).

[54] S. Biermann, A. Poteryaev, A. I. Lichtenstein, and A. Georges, Dynamical Singlets and Correlation-Assisted Peierls Transition in VO_2, Phys. Rev. Lett. **94**, 026404 (2005).

[55] H. W. Verleur, A. S. Barker, and C. N. Berglund, Optical properties of VO_2 between 0.25 and 5 eV, Phys. Rev. **172**, 788 (1968).

[56] S. Xu, X. Shen, K. A. Hallman, R. F. Haglund, and S. T. Pantelides, Unified band-theoretic description of structural, electronic, and magnetic properties of vanadium dioxide phases, Phys. Rev. B **95**, 125105 (2017).

[57] S. Shin, S. Suga, M. Taniguchi, M. Fujisawa, H. Kanzaki, A. Fujimori, H. Daimon, Y. Ueda, K. Kosuge, and S. Kachi, Vacuum-ultraviolet reflectance and photoemission study of the metal-insulator phase transitions in VO_2, V_6O_{13}, and V_2O_3, Phys. Rev. B **41**, 4993 (1990).

[58] Y. Hinuma, G. Pizzi, Y. Kumagai, F. Oba, and I. Tanaka, Band structure diagram paths based on crystallography, Comput. Mater. Sci. **128**, 140 (2017).